J. Fluid Mech. (2000), *vol.* 424, *pp.* 45–73. Printed in the United Kingdom

Mixing and entrainment in developing stratified currents

By G. PAWLAK[1] AND L. ARMI[2]

[1]School of Oceanography, University of Washington, Seattle, WA 92195-7940, USA

[2]Scripps Institution of Oceanography, University of California, San Diego, La Jolla, CA 92093-0230, USA

(Received 3 December 1999 and in revised form 1 May 2000)

The spatially developing region of a steady downslope current in transition from a hydraulically controlled, arrested wedge flow is examined through a set of laboratory experiments. The mixing and entrainment mechanisms at the shear interface are explored with the use of imaging techniques. The initial, unstable accelerating region, characterized by rapid development, low shear layer Richardson numbers and high entrainment rates, is limited by the effects of stratification which suppress the large-scale overturning. A subsequent high Richardson number region is characterized by weak entrainment and the collapse of turbulence from the initial region. The flow approaches a quasi-stable state as the mixed layer draws energy from the accelerating density current. Observed large-scale structure is attributed to an instability of the marginally unstable shear layer. Entrainment rates are calculated within each region for the various slopes considered and estimates for the extent of the transition regions are obtained.

1. Introduction

The flow of a dense fluid along a sloping bottom is a basic geophysical process in scenarios ranging from deep ocean outflows to downslope mountain winds. Gravity currents also provide an important mechanism for transfer of sediments. The establishment of these flows in many cases derives from a region of hydraulic control due to a geometric constriction, which generates selective acceleration of the stratified fluid. This acceleration in turn destabilizes the flow to shear instabilities that result in turbulent mixing and transfer of mass and momentum.

Numerous observational studies exist which document the occurrence of these downslope flows in the atmosphere and ocean. Lilly (1978) and Nieman *et al.* (1988) examined separate downslope windstorms in Colorado. Recent work by Farmer & Armi (1999) draws analogies between these mountain wind events and their observations of flow over a sill in Knight Inlet in British Columbia. Baringer & Price (1997) have explored the development and entrainment of the Mediterranean outflow at the west end of the Strait of Gibraltar.

From the experimental approach, a significant body of work has been generated addressing the transient gravity current problem. The steady flow situation, however, has received less attention following the classic set of experiments by Ellison & Turner (1959). A notable exception is the recent work by Baines (1998) who examined downslope flows into a stratified environment. The study by Ellison & Turner, motivated by the problem of buoyant flow of methane gas along the roof of a mine shaft, examined the entrainment of a developed stratified current along a slope. They

found that the entrainment of ambient fluid into the flowing layer was proportional to the layer velocity and an inverse overall Richardson number (or equivalently, the layer Froude number) for the layer. The variation of the entrainment with bottom slope was essentially linear.

Their examination of the theory for inclined plumes showed that for a constant slope, the flow reaches a constant Richardson number through a balance between gravity, bottom friction and entrainment, within an estimated distance of $10h_o$, where h_o is the initial layer depth. As a consequence, the effect of this initial transition region was justifiably neglected in their experiments. In many flows, however, this initial adjustment region may contribute a significant portion of the local mixing, as is suggested by the vigorous mechanisms evidenced in Pawlak & Armi (1998). Additionally, variations in bottom slope or channel width create regions of local hydraulic readjustment which will alter the flow balance and entrainment mechanisms. Baringer & Price (1997) reported increased entrainment in regions of increased slope in the Mediterranean outflow.

The turbulent structure in inclined plumes has remained largely unexplored, although Ellison & Turner described 'irregularities or turbulent eddies' in the downslope flow. Observations of periodic gusts in downslope windstorms have been widely reported. Lidar observations by Nieman *et al.* (1988) of a downslope windstorm showed evidence of large-scale coherent structure advected by the mean wind. Peltier & Scinocca (1990) have used numerical simulations of downslope winds to relate Kelvin–Helmholtz instabilities to these periodic gusts. The nature of the entraining process and the mechanism for instability in a developed downslope current have not been examined, however.

In an earlier paper (Pawlak & Armi 1998) we examined the initial stages of development in the accelerating, stratified shear layer which occurs within the arrested wedge flow. A new type of vortex mechanism was observed which was shown to be a result of the spatial acceleration of the flow, coupled with the effects of buoyancy on the inclined mixing layer.

The general goal of the present study is to understand, qualitatitively and quantitatively, the small-scale mixing processes at work in oceanic settings such as Knight Inlet and the Strait of Gibraltar, as well as atmospheric flows over topography. In addition, we will use the developing downslope current to examine the characteristics of stratified turbulence.

The hydraulic flow of two homogeneous layers of differing densities through variations in geometry is described in general in Armi (1986). Wedge flows are a special case of two-layer exchange flows, occurring when the net barotropic flow through the channel exceeds a critical value, such that only one layer can flow. These are discussed for flow over a sill in Farmer & Armi (1986). The flow is critical to long internal waves at the sill crest (intermediate barotropic flow) or at the tip of the wedge (strong barotropic flow). Arrested wedges in a channel with a contraction were considered in Pawlak & Armi (1997) including the effects of friction and cross-stream non-uniformity. The experiments we will present fall within the intermediate barotropic flow regime, with a flowing lower layer, for which the tip of the wedge reaches upstream of the sill crest. The upstream (relative to the direction of net barotropic flow) portion of the wedge is subcritical to long internal waves and the flow transitions to supercritical conditions downstream, passing through a hydraulic control at the sill crest. The flowing layer continues to accelerate downstream in response to the increase in depth.

A complication of the earlier study was the width variation in the channel which

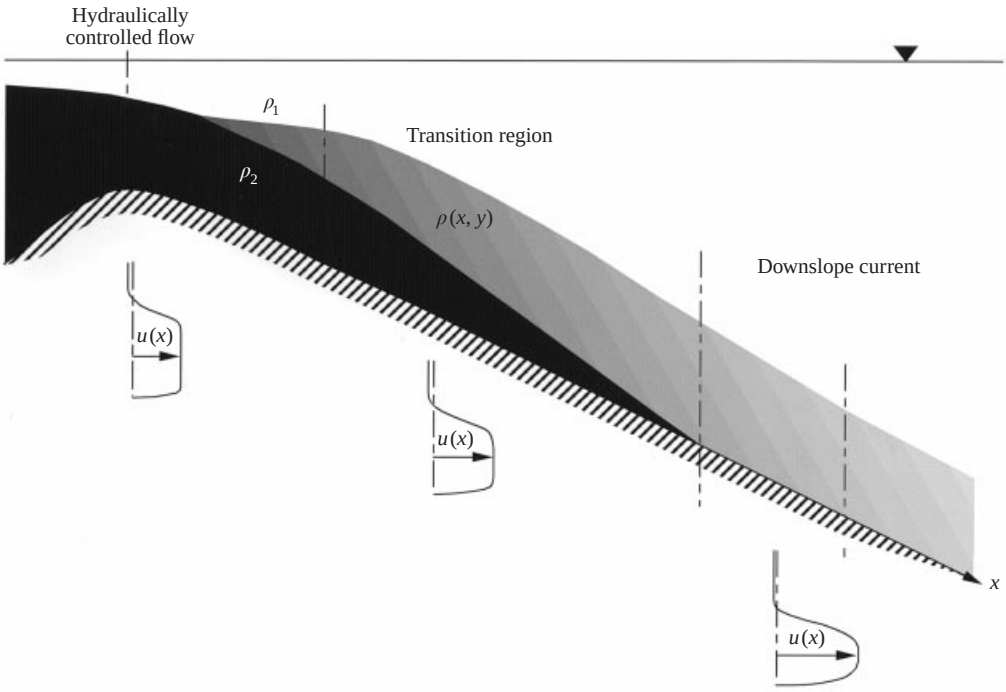

FIGURE 1. Sketch of hydraulic flow in transition to a downslope current.

introduced cross-stream vortex stretching into the shear flow. One of the intentions of the current experiments was to examine the initial developing region in a parallel wall channel. A further goal was to examine the fully developed region of the mixing layer in the hydraulically controlled, arrested wedge flow and to explore the transition of the hydraulic flow to a downslope current. In this paper then, we shall investigate the effects of acceleration and buoyancy on the structure and development of the mixing layer and, in turn, examine how these effects modify the entrainment and mixing of fluid from either layer. Furthermore, we shall consider the plunging, accelerating mean flow from the perspective of a developing downslope current. For a sufficiently long incline, the flowing layer will eventually attain an equilibrium state in which a balance between kinetic energy production and frictional losses is maintained. It is at this stage that the flow attains a steady Richardson number and constant velocity as shown by Ellison & Turner. The mixing and entrainment occurring in the development region is then the key to the establishment of the density gradients that drive the flow.

Several dynamically distinct regions will be identified in the evolution of a downslope current along a constant slope, from a hydraulically controlled flow. Figure 1 illustrates the various regimes of the mean flow of interest. Associated with the hydraulic control, involving a transition from subcritical to supercritical flow, is the initial acceleration of the flowing layer. The subsequent increase in shear destabilizes the interface to vorticity instabilities. The first important segment in the developing downslope current is the region of initial instability. The interfacial instability in this region has not yet reached a scale that is significantly affected by buoyancy so that entrainment and mixing remain high. Buoyancy becomes a dominant mechanism in the second region, limiting the scale of instabilities in the mixed layer. The flow continues to accelerate downstream in hydraulic response to the increasing depth.

Mixing is reduced relative to the first region, but the input in energy resulting from the acceleration leads to further development of the mixed layer. The third and final region downstream is the establishment of the steady downslope flow. A balance between inertial and frictional forces is attained and mixing continues to be weak due to the effects of buoyancy.

In this study we shall ignore the influence of the bottom boundary layer on the mixing at the interface. We note, however, that a rough bottom or an otherwise separating boundary layer will significantly alter the nature of the turbulent flow and the entrainment mechanisms at the interface.

In the following section we will describe the experimental facility along with the diagnostic techniques used. Section 3 presents an overview of the properties of the mean downslope flow. In § 4 we will focus on one experimental case to examine details of the structure within the developing downslope current in order to shed light on entrainment mechanisms. Details of the fluctuating velocity field are considered in § 5 and entrainment rates are presented in § 6.

2. Experimental facility and diagnostics

To examine the more highly developed region of the arrested wedge flow, experiments were conducted in a modified version of the facility described in detail in Pawlak & Armi (1998). The facility, illustrated in figure 2, consists of a rectangular Plexiglas channel, approximately 2 m in length, connecting two 800 l reservoirs. The channel cross-section is 30 cm high and 15 cm wide. A variation in channel cross-section is introduced using a Plexiglas sill, shown in figure 2(*b*). The upstream portion of the sill consists of a 45 cm smoothly varying section extending 5 cm beyond the crest of the sill. The downstream part of the sill consists of a flat Plexiglas plate providing a constant slope between the first half of the sill and the channel bottom. Various slopes were considered by using different length plates attached as shown in figure 2(*b*). The experiments discussed herein used plates of 60 cm, 80 cm, 120 cm and 220 cm in length giving slope angles of 14.5°, 10.8°, 7.2° and 3.9°, respectively.

The arrested wedge flows are experimentally established as discussed in Pawlak & Armi (1998). Density variations were obtained using salt, with temperatures monitored in each tank to ensure isothermal conditions. A sliding gate at one end of the channel initially separates the two reservoirs. To begin the experiment, the gate is lifted and a known net barotropic flow is then generated in the channel by pumping dense salt water from the layered reservoir to the other with calibrated pumps. Open-cell foam diffusers were placed in each tank as well as in the upstream section of the channel in order to eliminate velocity fluctuations generated by the pumping.

Since flow velocities for hydraulically controlled flows scale with $\sqrt{g'h_0}$, where h_0 is the depth at the sill crest and $g' = g\Delta\rho/\rho$ is the reduced gravity, the decrease in depth over the prior experiments meant that the density difference had to increase to maintain velocities at levels of interest. This factor, combined with the increase in channel width from 7.5 cm at the narrowest section in Pawlak & Armi (1998) to a constant-width 15 cm channel, required that the resulting net flow rate necessary to maintain the arrested wedge flow must also increase. The run time for the facility scales inversely with the flow rate, so to account for the increase in flow rate, a third tank was added as a buffer between the downstream and upstream reservoirs. Water was then pumped from the bottom of the downstream reservoir through a set of diffusers near the top of the buffer tank, which was connected at the bottom to the upstream tank by a large (10 cm) diameter duct. This setup also allowed the

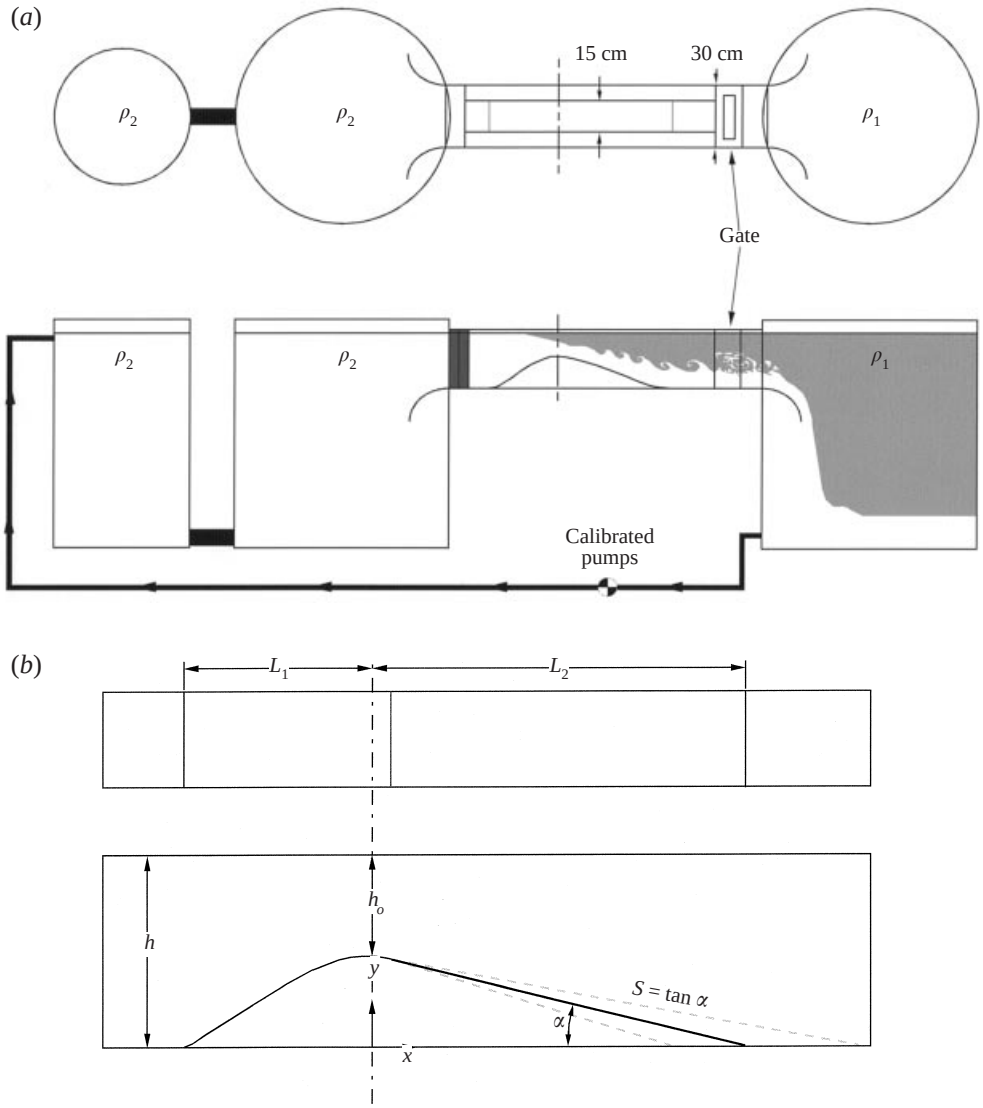

FIGURE 2. (*a*) Experimental facility. (*b*) Channel details showing sill geometry.

downstream tank to be initially filled with a larger quantity of fresh water, preventing a layer of mixed fluid from intruding upstream into the test section as the experiment progressed. With these modifications, run times were maintained at about 20 to 25 min beyond the 5 to 10 min initial transient time.

Imaging techniques were used in diagnosing the flow, including laser induced fluorescence (LIF) for flow visualization and density field measurements, as well as digital particle imaging velocimetry (DPIV) for measurement of the velocity and vorticity fields. The methods used for these are essentially the same as those outlined in Pawlak & Armi (1998), with the exception of the following improvements to the DPIV system. The particle field images were obtained using a full frame 480 $\times$ 640 pixel camera allowing increased vertical resolution and accuracy. In addition, the concentration of rhodamine dye in the lower layer was reduced to increase the

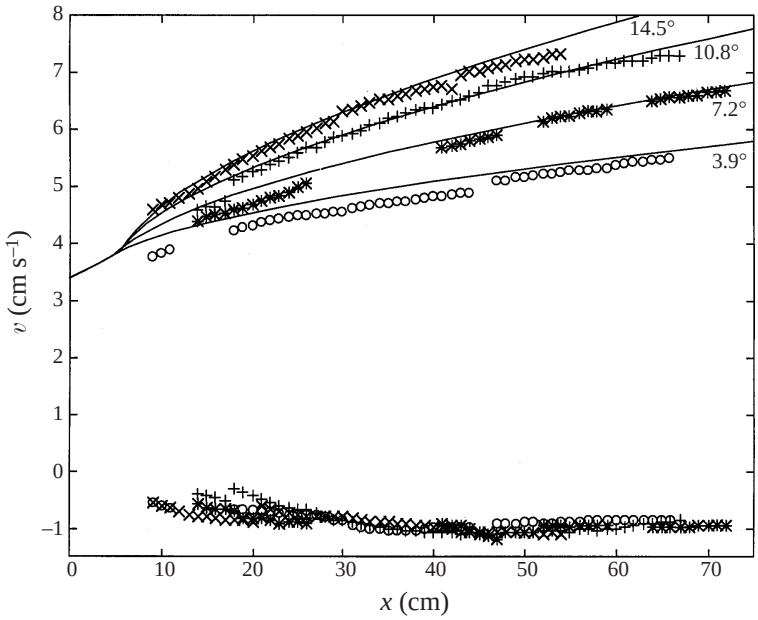

FIGURE 3. Experimental velocities. The corresponding bottom slope angle, α, is given for each plot symbol along with the predictions of hydraulic theory for the flowing layer velocity. Negative values are upper layer velocities.

contrast with particles, thus eliminating the need for any image processing prior to the DPIV processing.

A standard, interlaced CCD camera was fitted with a light filter to exclude light at the laser frequency, allowing measurement of the density field from the fluorescence of the rhodamine dye. The imaged region for the density measurements was typically about 18.5 cm by 14 cm. The full frame DPIV camera was focused on a smaller region of about 16 cm by 12 cm, overlapping that of the first camera, permitting simultaneous measurement of velocity and density fields.

3. Mean properties

A range of accelerations was considered by varying the downstream slope of the sill as discussed in § 2. In this section, we will present averaged flow quantities versus downstream position referenced from the sill crest. These will not be non-dimensionalized as is customary for shear flows, since there is no single non-dimensional parameter for downstream distance in a spatially accelerating flow.

Averaged maximum free-stream velocities for the flowing layer, obtained from DPIV analysis, for the four slopes considered, are summarized in figure 3 as the positive velocities. Experimental velocities represent averages over time series of 100 s with typical sampling frequencies of 1.5 Hz. The theoretical curves from the predictions of hydraulic theory for flow over a sill, including effects of flow non-uniformity and laminar frictional losses (Pawlak & Armi 1997), are also included in figure 3. Maximum upper-layer velocities for all slopes considered (negative values) range from zero near the wedge tip region, increasing in magnitude through the initial unstable region to about 1 cm s^{-1} downstream. This weak backflow occurs in the upper layer due to the effects of viscous diffusion and turbulent entrainment along the interface.

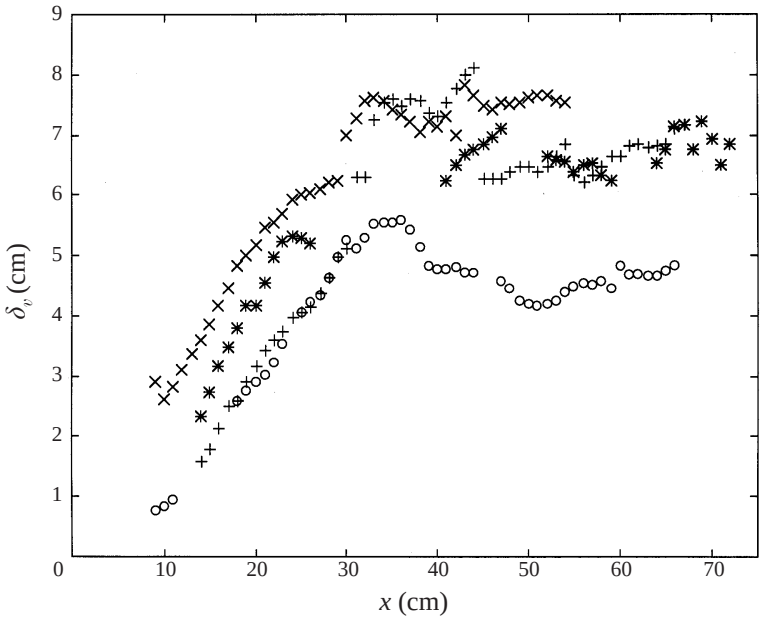

FIGURE 4. Vorticity thickness, δ_v vs. x, symbols are as given in figure 3.

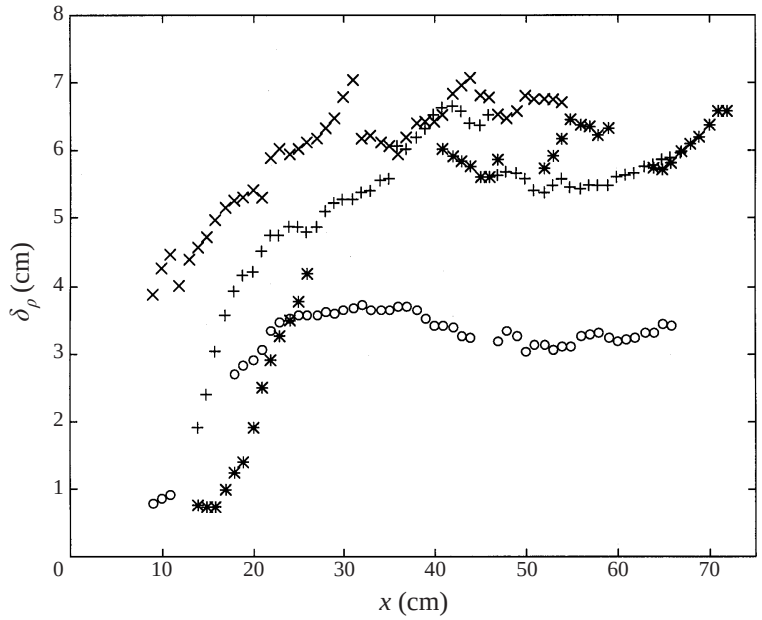

FIGURE 5. Density thickness, δ_ρ vs. x, symbols are as given in figure 3.

The evolution of the mixed-layer thickness with downstream distance can be examined with both the velocity field data and averaged density profiles. The density field was obtained from 90 s image sequences at a frequency of 3 images per second. Figures 4 and 5 show the variation of the vorticity thickness, δ_v, and the density thickness, δ_ρ, respectively, for all slope angles considered. The vorticity thickness,

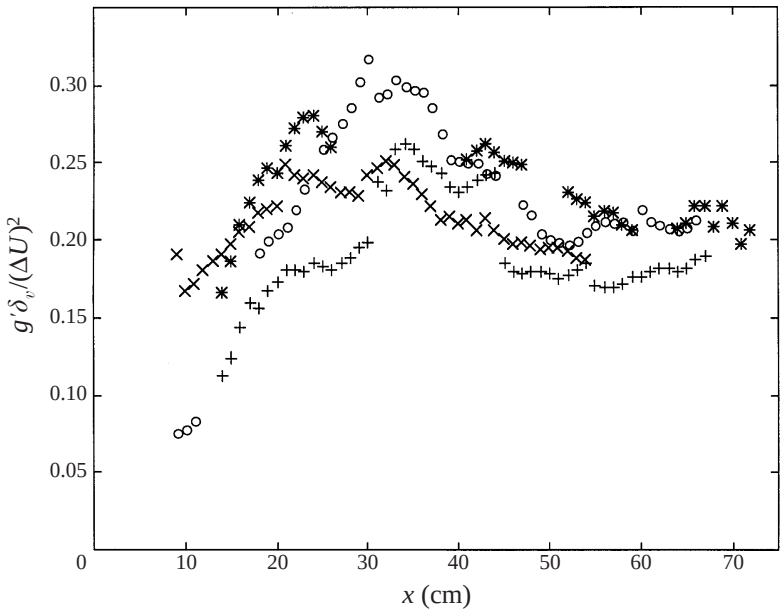

FIGURE 6. Bulk Richardson number, J vs. x, symbols are as given in figure 3.

δ_v, was obtained from the inverse slope of the best-fit line through the normalized velocity profile between the 15% and 85% values,

$$\delta_v = \left(\overline{\frac{\mathrm{d}\bar{v}}{\mathrm{d}y}\Big|_{\bar{v}(y)=0.15}^{\bar{v}(y)=0.85}} \right)^{-1}, \tag{3.1}$$

where $\bar{v}$ is the velocity normalized by the local velocity difference. The density thickness, δ_ρ, was similarly defined using the normalized density profiles. Two distinct regions of mixed-layer development are identifiable from the data in figures 4 and 5. An initial region of rapid spreading is evident between $x = 0$ and 30 cm, followed by a region of very low growth rate.

The overall Richardson number defined by

$$J = \frac{g'\delta_v}{(\Delta U)^2} \tag{3.2}$$

plotted in figure 6 for all experimental cases shows a steady increase in the initial region approaching the stabilizing value of $O(0.3)$ (cf. Koop & Browand 1979; Corcos & Sherman 1976) and then decreasing slowly downstream. This evolution in Richardson number is typical for stratified mixing layers, in which the stabilization results from collapse and restratification. The variation in the maximum Richardson number evident in figure 6 is probably a result of slight variations in the initial mixed-layer thickness and its resultant Richardson number. Koop & Browand (1979) observed similar variations in maximum Richardson number, attributed to a discrete number of pairings possible in the stratified mixing layer.

In Pawlak & Armi (1998), the effects of acceleration on the initial region of the developing shear layer were parameterized using an acceleration parameter, defined as

$$T_A = \frac{\delta}{U}\frac{\mathrm{d}U}{\mathrm{d}x}, \tag{3.3}$$

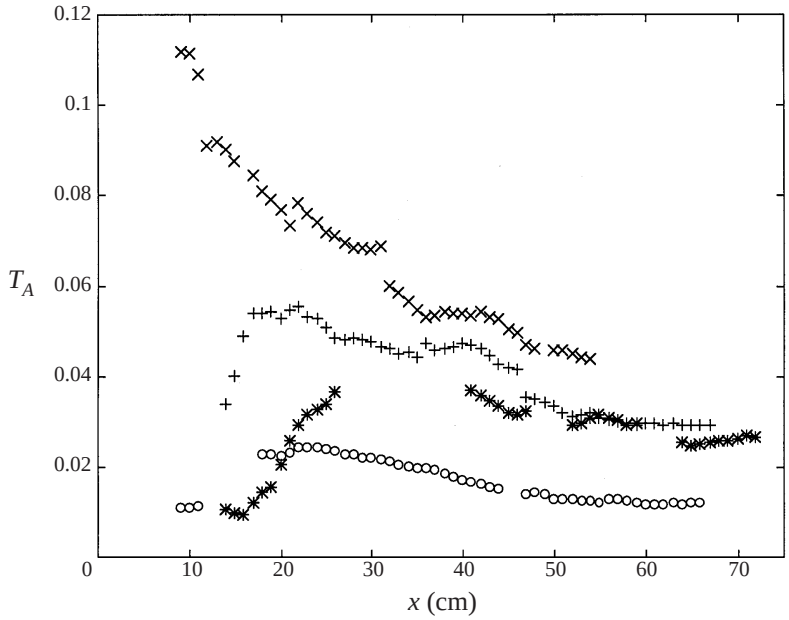

FIGURE 7. Acceleration parameter, T_A vs. x, symbols are as given in figure 3.

in which δ is some measure of the vertical scale of the shear layer and U is the free-stream velocity of the flowing layer. This parameter, which can be interpreted as a ratio of an eddy time scale to an acceleration time scale, then varies with downstream distance as the flow accelerates and as the mixing layer develops. Previously (in Pawlak & Armi 1998), T_A was defined using only the initial value of the momentum thickness, for the purpose of examining the initial development of the instabilities. In figure 7, we show the variation of T_A using $\delta = \delta_v$ to highlight the variation of the effects of acceleration with downstream distance as well as its variation over the experimental cases considered.

4. Flow structure

4.1. *High entrainment region*

The flow remained stable to interfacial instabilities in the upstream portion of the wedge. Measurements in this region indicate initial momentum thicknesses between $\delta_\theta = 0.2\,\text{cm}$ and $\delta_\theta = 0.5\,\text{cm}$, where δ_θ is defined as

$$\delta_\theta = \frac{1}{\Delta U}\int_{-\infty}^{\infty}(U - u(y))u(y)\,\mathrm{d}y, \tag{4.1}$$

with Reynolds numbers based on δ_θ from 80 to 230 for the four cases considered. The experimental facility provided a steady spatially developing shear interface, on which Kelvin–Helmholtz (K–H) instabilities appeared at a repeatable and regular interval between 10 and 20 cm downstream of the sill crest for all the experiments presented, without the need for any type of forcing.

Visualization of the initial region of instability reveals the prominence of the vortex dynamics detailed in Pawlak & Armi (1998). A sequence of images from the developing region is shown in figure 8. Instabilities evolve in an asymmetrical manner

FIGURE 8. Image sequence from the developing region. Corresponding vorticity images are shown to the right of each image. Sequence order is from top to bottom, continued in the second column.

with the developing cores pinching off into the low-momentum stream. The leapfrog pairing mechanism is prominent, in which a developing K–H billow separates from the primary density interface and skips over the second vortex in the subharmonic pair to interact with the third or fourth vortex upstream. The visualizations in these parallel-wall experiments indicate that the mechanism is, to first order, not affected by the vortex stretching produced in the variable-width experiments in Pawlak & Armi (1998).

The primary effect of the vortex dynamics examined by Pawlak & Armi (1998) is the generation of a strongly asymmetrical density profile. A subsequent selective entrainment of light fluid into the mixed layer was also evident in their study.

Figure 9 shows a composite of density gradient field images along with a sequence of velocity and density profiles, $u(y)$ and $\rho(y)$, illustrating the flow evolution for $\alpha = 10.8°$. The bottom slope has been removed and the resulting horizontal coordinate is the downslope distance. As is evident from the velocity profiles, the bottom boundary layer thickness remains small relative to the thickness of the flowing layer in the initial

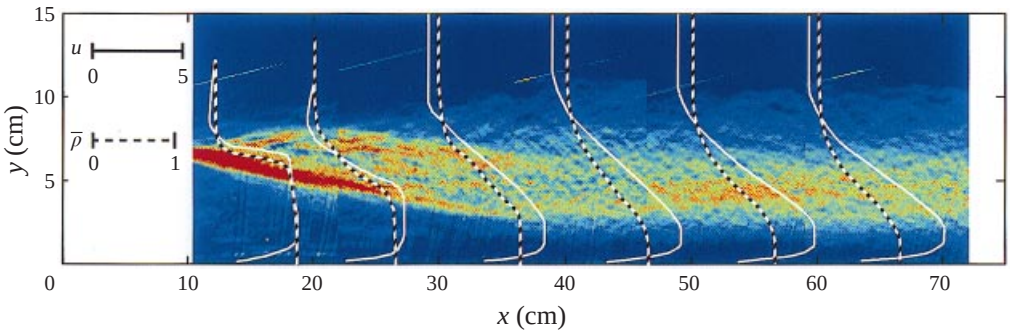

FIGURE 9. Evolution of velocity and density profiles superimposed on a composite of density gradient field images.

region. A significant core of inviscid flow remains and the assumptions of uniform, hydrostatic flow continue to yield a good prediction of the free-stream velocity (figure 3). As the flow develops further downstream, both the bottom boundary layer and the interfacial mixed layers become more prominent. The asymetrical development in the initial region is evident in the density gradient field for $x < 30$ cm, as discussed in Pawlak & Armi (1998). This is less evident as the flow progresses downstream.

The relative extent of the initial rapid growth region in the experimental domain is evident in figure 9. The low Richardson number region plays a limited role in the development of the steady gravity current. Although entrainment is high in this region, its growth becomes limited by the effects of stratification over a short distance. For hydraulically controlled single-layer flows, the velocity in the vicinity of the control scales as $U \sim \sqrt{g'H}$, where H is the height of the reservoir over the sill crest. This results in a bulk Richardson number for the interface, of $Ri = J\cos\alpha \sim \delta_v \cos\alpha/H$, where δ_v is the vorticity thickness. For a homogeneous turbulent shear layer, with one flowing layer, the vorticity thickness can be expressed as

$$\delta_v = \delta_x x + \delta_{v_0}, \tag{4.2}$$

where δ_x is the linear spreading rate of the mixed layer (cf. Brown & Roshko 1974). If we assume that $\delta_{v_0} \ll H$ and that α is small, then $Ri = \delta_x x/H$, and it follows that the shear layer reaches a critical Richardson number, $Ri_c = 1/4$ in a distance

$$\Delta x_1 = \frac{H}{4\delta_x}. \tag{4.3}$$

Koop & Browand (1979) showed that the stratified mixing layer grew as a homogeneous shear layer for $Ri < 0.32$, for which $\delta_x = 0.18$. The extent of the initial low Richardson number region is then limited to a length $\Delta x \sim O(H)$. In the experiments presented here, δ_{v_0} is set by viscous and surface tension effects such that the initial Richardson number is already a significant fraction of one quarter. In geophysical scenarios such as Knight Inlet (Farmer & Armi 1999), although viscous effects are negligible, a finite value for δ_{v_0} is prescribed instead by the hydraulic flow of the stratified fluid (Armi & Williams 1993). Since a true two-layer flow is rarely achieved in geophysical flows and the velocity profile and density profile are inextricably linked through the hydraulics, the stratified environment plays a similar role to that of the viscosity in establishing the initial velocity profile. Nonetheless, the $\Delta x \sim O(H)$ scaling will apply.

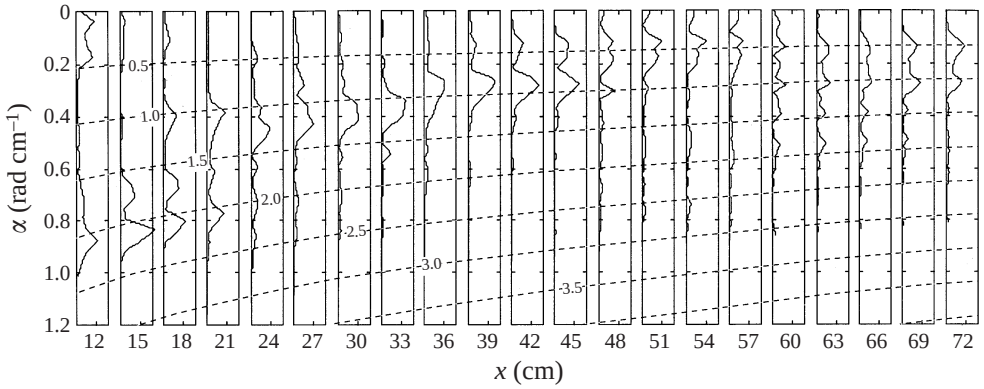

FIGURE 10. Downstream evolution of cross-stream-averaged spectra. Vertical axis is wavenumber, inferred from local mean velocity. Lines of constant frequency (rad s^{-1}) are superimposed.

4.2. *Low-entrainment developing region*

As is evident from the data presented in § 3, as well as in the composite image in figure 9, a significant change in the development of the mixed layer occurs after the initial rapid growth of interfacial instabilities. In the experiments presented herein, this occurs beyond about $x > 30$ cm. The overall Richardson number (figure 6) increases rapidly to near the stabilizing value of $O(0.3)$ after which the growth in shear layer thickness appears to be arrested. The collapse and subsequent restratification of the stratified shear layer is a well-documented process examined by Koop & Browand (1979) among others. They observed an initial rapid growth through vortex pairing of the shear layer much like in the unstratified case. As the Richardson number increased past a critical value as a result of the growth of the mixing layer by vortex pairing, the pairing mechanism was suppressed, the development of the layer ceased and production of turbulence in the shear layer died out, with the exception of turbulence generated by the restratification process.

Although the mixed layer in the transition to a downslope current rapidly reaches a stabilizing Richardson number (figure 6), visualizations of the interface region indicate that turbulent mechanisms still persist. Spectral analysis of the density field image sequences also shows evidence of the development of subharmonic modes well after the stabilizing Richardson number criterion has been reached. This is shown in figure 10 in which the downstream evolution of the wavenumber spectra for $\alpha = 10.8°$ was obtained by vertically averaging the spectra of the density time series at individual pixels. The wavenumber is obtained from the frequency assuming a convective speed of $\Delta U/2$. Lines of constant frequency illustrate the spatial spreading due to acceleration. The initial pairing is complete by about $x = 24$ cm. Lower frequencies near the second subharmonic become dominant beyond $x = 50$ cm with the wavenumber $k \approx 0.15$ rad cm^{-1} of the peak corresponding to a wavelength of $\lambda \approx 40$ cm!

Structures of this scale were not readily identifiable when examining image sequences in this region, since the spatial extent of the individual images was limited to about 10 cm. This limitation was overcome with a time series constructed from a vertical cut at a given location in the spatial image. Figure 11 shows a 70 s time series from $x = 53$ cm, which clearly reveals large-scale structure. A number of structures of long temporal extent can be identified. A spatial length scale can be inferred by as-

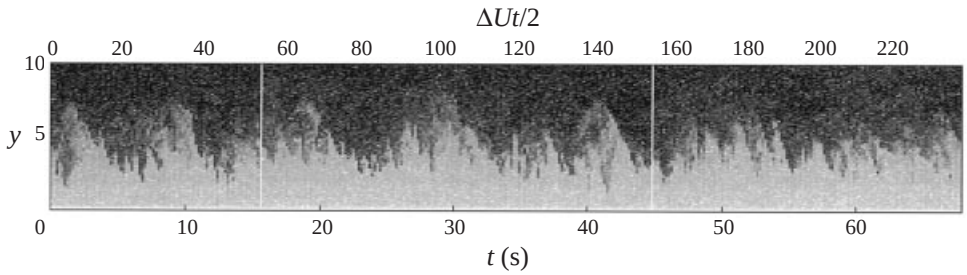

FIGURE 11. Temporal sequence from $x = 53$ cm, $\alpha = 11.8°$.

suming a convective velocity of $\Delta U/2$. Figure 12 shows an expanded view of a portion of the sequence. The images in figure 12 are scaled such that the aspect ratio reflects a one-to-one spatial scale using the inferred convective horizontal length scale. The accompanying vorticity and velocity fluctuations are shown below. The wavelength of the structures in figures 11 and 12 is approximately 40 cm, indicating that these correspond to the low-wavenumber peak in the spectral analysis. The image sequence in figure 12(*b*) shows individual spatial views at various phases within the large-scale structure. Small-scale Kelvin–Helmholtz instabilities are visible, developing within the larger mixed layer, concentrated primarily in the 'nodes' of the larger-scale structure.

Additional time series for the density fluctuations, similar to that in figure 11, were obtained simultaneously from vertical cuts at $x = 48.5$ cm and $x = 62.5$ cm. Cross-correlations were performed between the low-pass-filtered time series for pixels at equal heights from the bottom. The peaks in each cross-correlation yield convective velocities versus vertical position for low-frequency structures. These velocities inferred from the cross-correlations are plotted in figure 13 along with the mean velocity profiles from the two x-locations. The plot suggests that the flow structure throughout the depth of the shear layer is essentially advected with the mean velocity.

The solid vertical line represents the velocity obtained from the mean of the cross-correlations at each pixel, shown in figure 14. The initial peak corresponds to the passage of an individual structure past the two locations at a time lag of $\Delta t = 4.0$ s. The peaks at about 15, 25 and 35 s in the plot illustrate the persistence of these structures, also seen in figure 11, at a period of $T \simeq 10.5$ s. A similar analysis with velocity fluctuations gives identical results. In § 7 we will attribute the low-frequency structure seen here to a forced instability on the marginally stable accelerating shear layer.

5. Velocity fluctuations

Velocity fluctuations were examined with the use of time series from PIV measurements. The streamwise r.m.s. velocity fluctuations, u'_{rms}, are plotted versus downstream position in figure 15, normalized by the mean shear, ΔU. Values remain steady in the initial, low Richardson number region and decay downstream as the initial turbulence collapses. The observed rate of decay in the downstream region agrees well with the slope of $x^{-3/4}$ noted by Koop & Browand (1979) in the collapsing stratified shear layer. One might expect a somewhat smaller rate of decay due to the input of energy from the accelerating layer and, indeed, a lower slope might be observed from the data; however, the variation in the data is too great to draw any definite conclusions.

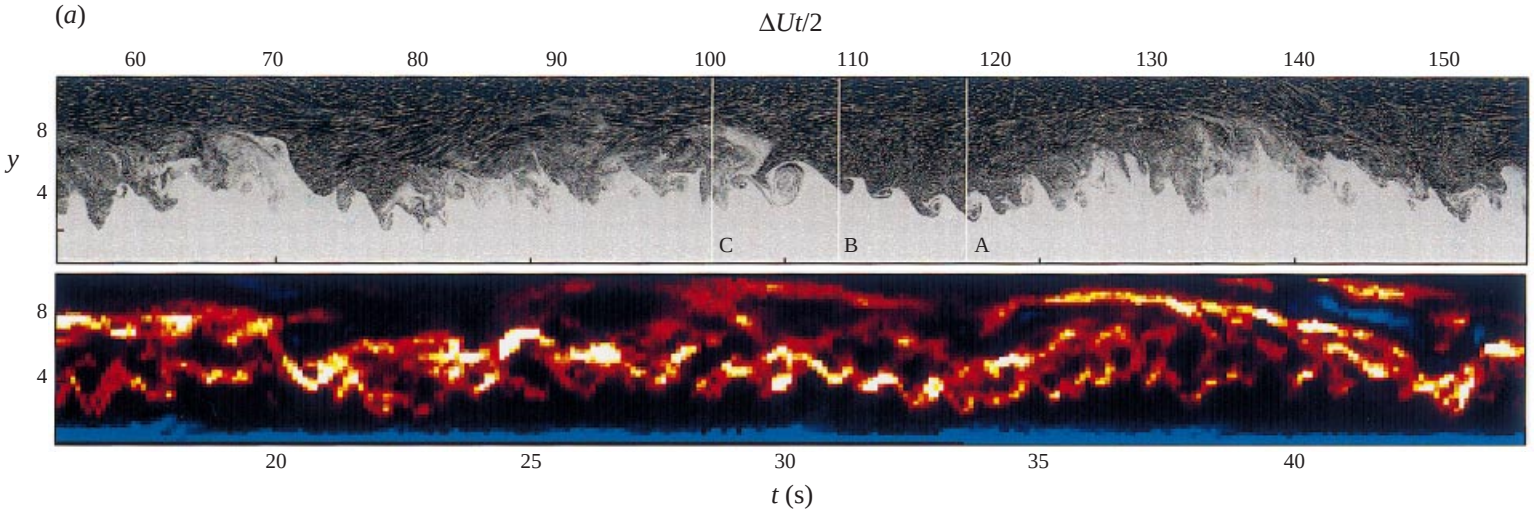

FIGURE 12. For caption see facing page.

(*b*)

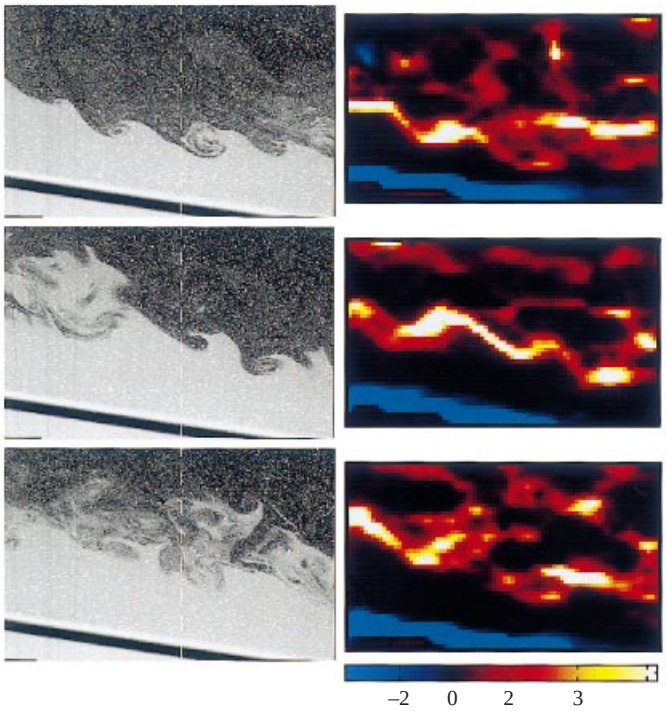

FIGURE 12. Temporal sequence from $x = 53\,\text{cm}$, $\alpha = 11.8°$. (*a*) y,t view of intensity and vorticity time series. (*b*) Selected spatial views from points A, B and C in (*a*). Corresponding vorticity images are shown at the right.

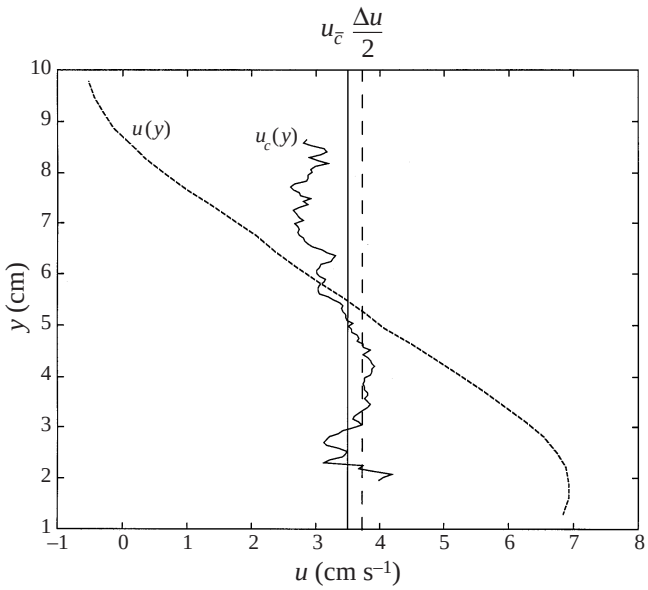

FIGURE 13. Convective velocities from cross-correlations of low-pass-filtered density fluctuations.

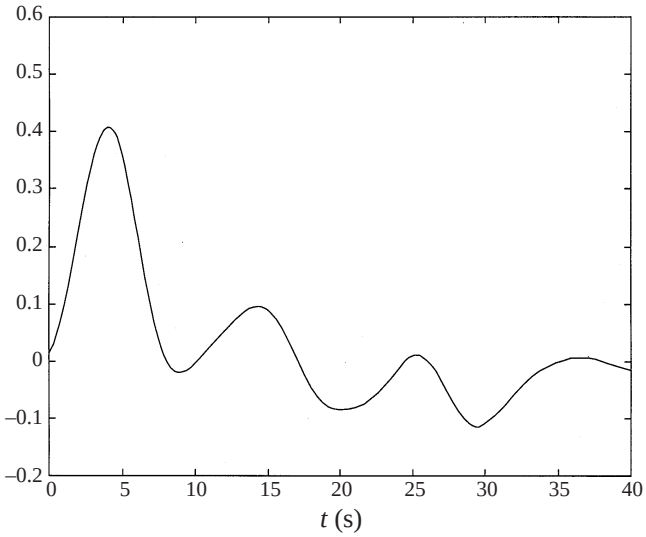

FIGURE 14. Vertical mean of cross-correlations in density fluctuations at $x = 48.5$ and 62.5 cm.

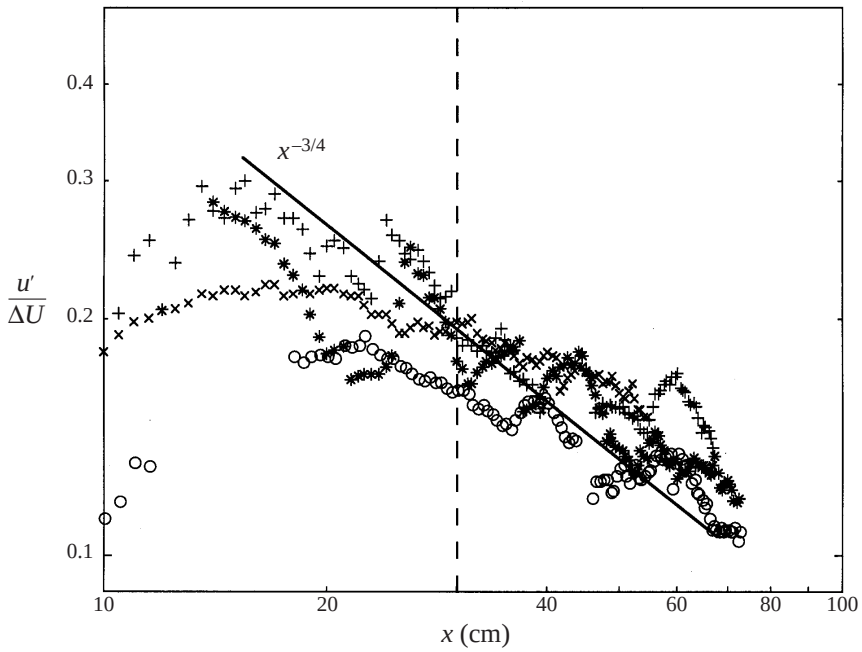

FIGURE 15. Maximum r.m.s. velocity fluctuations normalized by the mean shear vs. x. Symbols are as given in figure 3.

Some sense of the limiting effects of buoyancy on the velocity fluctuations can be obtained by comparison of the scales of the motions to a relevant density scale. Figure 16 shows $F_{rms} = u'_{rms}/\sqrt{g'\delta_\rho}$ versus downstream position. This quantity can be interpreted as the ratio of a time scale for the velocity fluctuations, u'/δ_ρ, to a buoyancy time scale, $\sqrt{g'/\delta_\rho}$. The data for each case suggest an asymptotic value of roughly one third for F_{rms}. Using δ_ρ as a length scale for the r.m.s. fluctuations however,

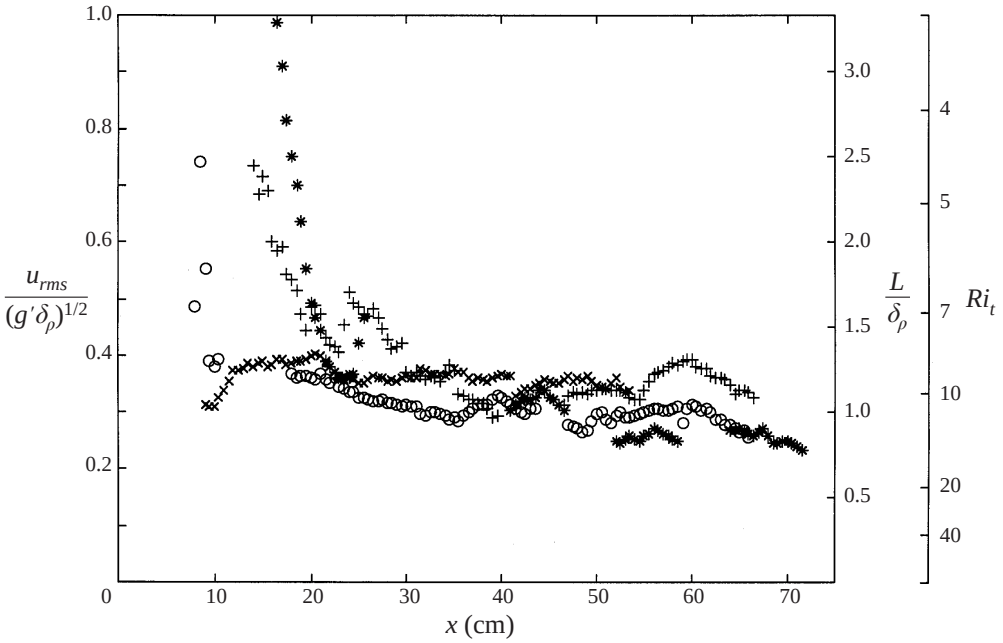

FIGURE 16. RMS Froude number vs x. Axes on right also show scale for the normalized turbulence scale and the turbulent Richardson number. Symbols are as given in figure 3.

is somewhat arbitrary since this implies that u'_{rms} represents scales of the order of the mixed-layer thickness. While this may apply in the initial high-entrainment region, one might expect that buoyancy will limit these motions within a 'collapsing' shear layer.

It has been observed by various authors (e.g. Hopfinger 1987; Thorpe 1982) that motions in decaying stratified turbulence are such that $u'/NL = 0.3$, where $N = \sqrt{g(\mathrm{d}\rho/\mathrm{d}z)/\rho}$ is the buoyancy frequency and L is an integral scale for the fluctuations. If we assume that this scaling applies, we find

$$\frac{L}{\delta_\rho} = \frac{1}{0.3}\frac{u'_{rms}}{\sqrt{g'\delta_\rho}} = \frac{1}{0.3}F_{rms} \tag{5.1}$$

using $N = \sqrt{g'/\delta_\rho}$. This ratio is also given in figure 16, using the first scale on the right. This scaling yields a turbulent length scale that is indeed comparable with the mixed-layer thickness in the downstream high Richardson number region.

We can additionally interpret this inferred scaling for the integral turbulent length scale as a Richardson number for the fluctuations:

$$Ri_t = \frac{g'L}{u'^2_{rms}} = \frac{1}{0.3}\frac{1}{F_{rms}}. \tag{5.2}$$

This quantity is given by the rightmost scale in figure 16. The asymptotic value for this turbulent Richardson number is approximately 10 for all cases.

We can get some idea of the relative contributions to u_{rms} from the energy spectra of the velocity fluctuations. Figure 17 shows representative frequency spectra of vertical and horizontal velocity fluctuations at $x = 52$ cm for $\alpha = 11.8°$. The plots are obtained by averaging spectra of velocity time series for all vertical positions at this x-location. Since frequencies at separate vertical positions represent different scales

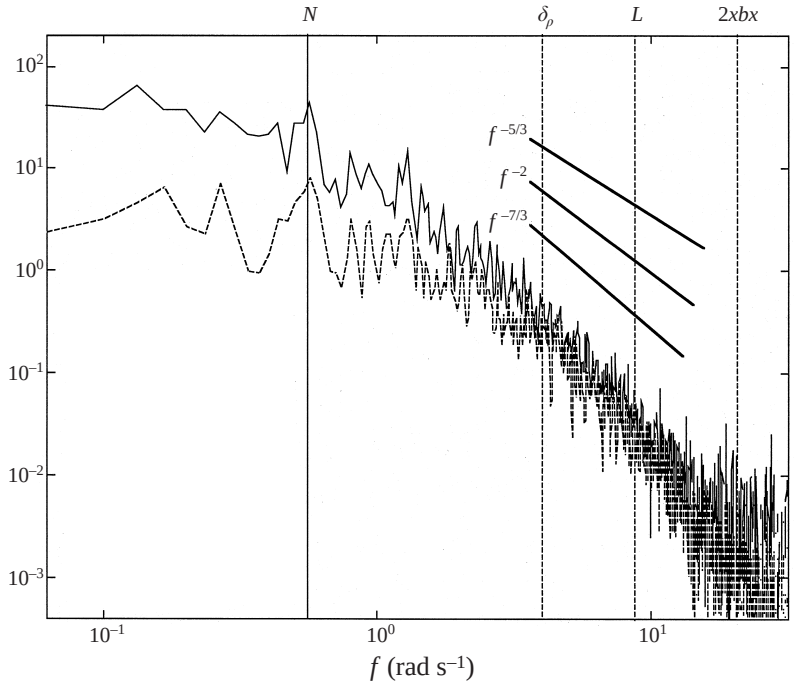

FIGURE 17. Spectrum for horizontal (solid line) and vertical (dashed line) velocity fluctuations at $x = 52$ cm for $\alpha = 11.8°$.

because of varying local convective velocities, frequencies in figure 17 are not all directly convertible to wavenumbers. Larger scales, which, as we have shown in § 4.2, extend across the flow and convect with the mean velocity, will be well represented in the frequency spectra. Smaller scales appear as lower frequencies in the slower regions of the flow and as higher frequencies in the faster regions. Analysis of spectra corrected for local mean velocities shows no discernable change in spectral shape or slope for the higher frequencies, however.

Using the convective velocity of $\Delta U/2$ observed for the large scales (§ 4.2) we can obtain various frequencies from the relevant length scales in the flow. The first important point to note is that the frequency of the large-scale structures coincides with the buoyancy frequency, N. We will address the significance of this observation in § 7. The spectra also contain a distinct peak at this frequency. Spectral levels at frequencies corresponding to the mixed-layer thickness, δ_ρ, and the inferred integral length scale, L, advected by the mean shear, suggest that the major contributions to u_{rms} are from the larger, buoyancy-affected scales. Slopes of $-7/3$ and -2 are shown for comparison along with the typical turbulent spectral slope of $-5/3$. The slope of the energy at frequencies above N is best described by the $-7/3$ line.

The effect of buoyancy is seen in the vertical velocity fluctuations at the larger scales where the energy is an order of magnitude less than that of the horizontal fluctuations. In addition, the energy at the smallest scales also shows a divergence. Despite the fact that at these scales the limits of the PIV averaging becomes significant, there is a distinct separation in the energy of the fluctuations of the smaller scales. This may be attributed to the intermittency of entraining vertical fluctuations which will be discussed further in § 7.

6. Entrainment

Given velocity and density field data, we can obtain estimates of the entrainment rates of fluid into the mixed layer from the high- and low-momentum streams. Following Ellison & Turner (1959) we define the entrainment rate, E, as

$$E = \frac{1}{V}\frac{\mathrm{d}Q}{\mathrm{d}x}, \tag{6.1}$$

where Q is the flow rate within the layer of interest and V is a representative velocity for the layer.

The choice of boundary definition for the individual layers is important in minimizing error and will be crucial in comparisons of entrainment rates from various data sets. We will use the density thickness, δ_ρ, defined in § 3 as the slope of the best-fit line through the normalized density ($\bar{\rho}$) profile between the 15% and 85% values. The vertical position where this line intersects the $\bar{\rho} = 0$ and $\bar{\rho} = 1$ values will represent the mixed-layer boundaries. The normalized total volume flux (per unit width) within the mixed layer can then be obtained as

$$Q = \frac{1}{H\sqrt{g'H}}\int_{y_H}^{y_L} v(y)\,\mathrm{d}y, \tag{6.2}$$

as well as the individual mass fluxes of high- and low-momentum stream fluid:

$$\left.\begin{aligned} Q_H &= \frac{1}{H\sqrt{g'H}}\int_{y_H}^{y_L} \bar{\rho}(y)v(y)\,\mathrm{d}y, \\ Q_L &= \frac{1}{H\sqrt{g'H}}\int_{y_H}^{y_L} (1-\bar{\rho}(y))v(y)\,\mathrm{d}y, \end{aligned}\right\} \tag{6.3}$$

where y_H and y_L are the high- and low-momentum stream boundaries for the mixed layer, respectively. These quantities are plotted in figure 18. The upper plots, (*a*) and (*b*), reflect the fact that the lower-density, upper-layer fluid is generally slower moving and thus has a lower volume flux. The three plots show the general increase in volume flux as acceleration or, equivalently, slope angle, increases. Also apparent in the data is the sharp change in volume flux slope between 20 and 30 cm as the effects of buoyancy are felt within the mixing layer.

Entrainment rates of either fluid into the mixing layer can be obtained using (6.1) given slopes from the data in figure 18. As is evident in the data, however, a direct calculation of the gradient would be difficult to interpret. A primary source of error in these estimates for the mass flux gradient results from the slow variation of the origin of the instabilities. The initial point of finite-amplitude development in each experiment varied within ± 10 cm over the course of several minutes. This introduces a positioning error into the data, which is always referenced to the sill crest. Since the data are taken in windows of several minutes, an image such as that shown in figure 9 represents composite sets of data which may be slightly shifted relative to each other. These errors are compounded in the entrainment rates which rely on gradient estimates. To minimize this difficulty, estimates of slope for the data in figure 18 were obtained using only neighbouring data points corresponding to velocity and density measurements taken concurrently.

From the perspective of a developing downslope current, the primary entrainment rate of interest is that of low-momentum fluid into the flowing fluid (figure 18*a*) so we will focus our attention on that quantity. Downward entrainment rates versus x are given in figure 19, obtained using equation (6.1) with V given by an integral-layer

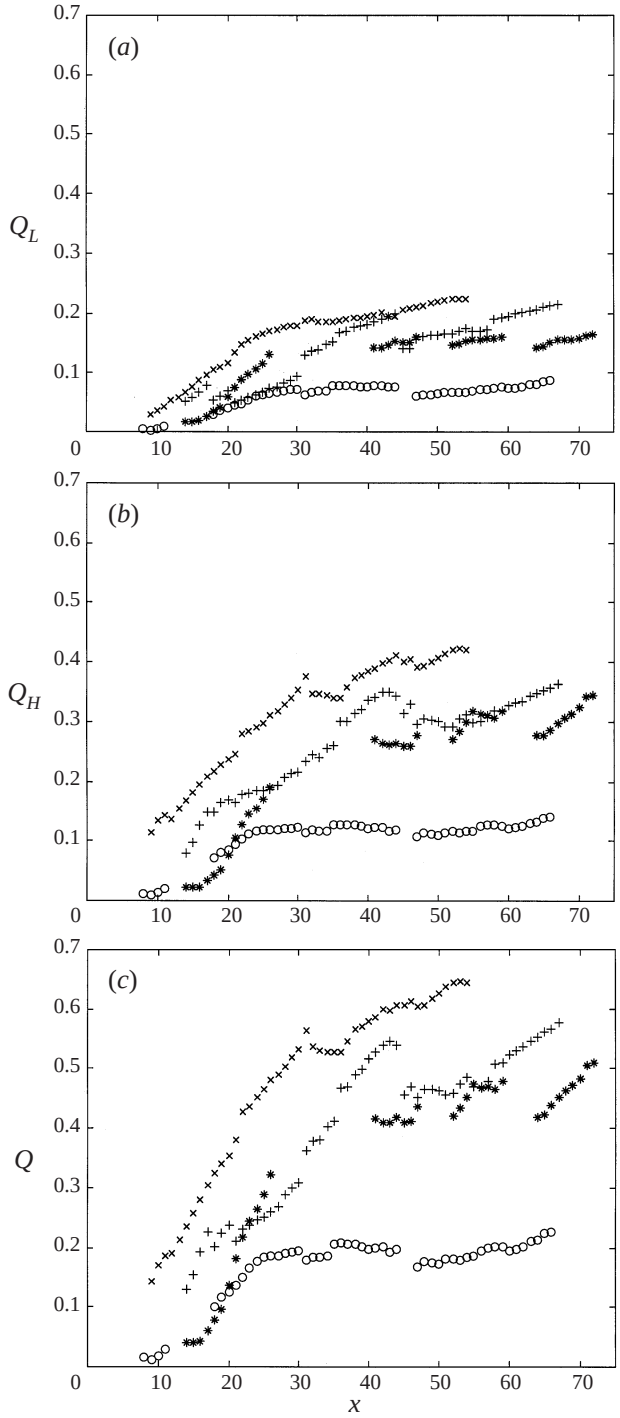

FIGURE 18. Mixing layer normalized mass flux rates vs. x: (*a*) upper-layer fluid, (*b*) lower-layer fluid, (*c*) total mass flux. Symbols are as given in figure 3.

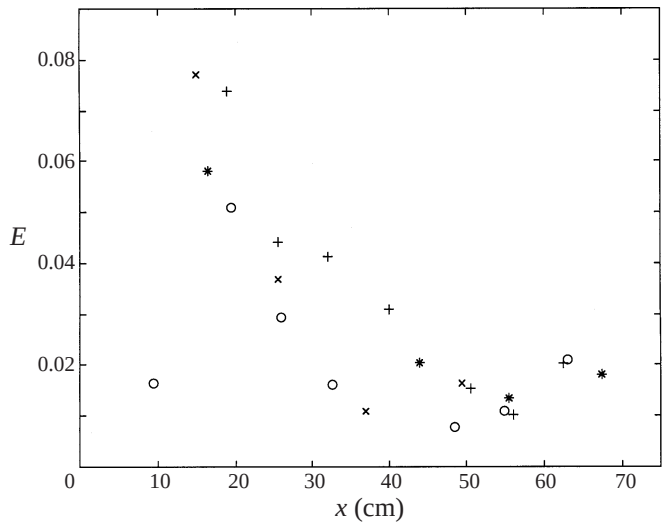

FIGURE 19. Downward entrainment rate of lower-layer fluid vs. x.

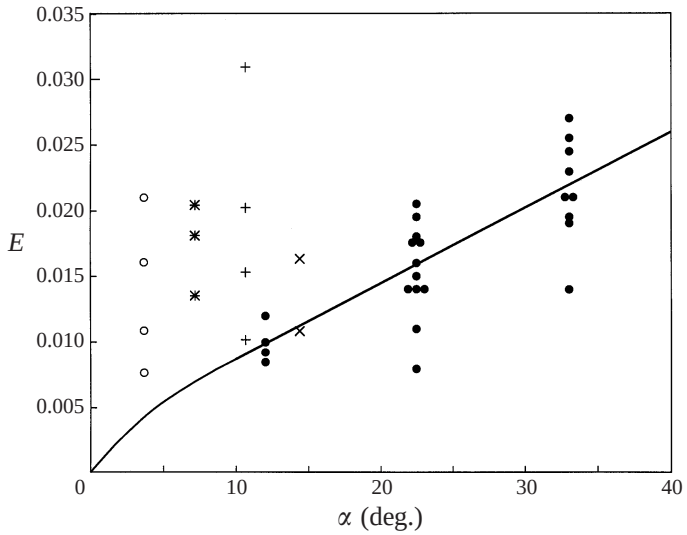

FIGURE 20. Entrainment vs. slope angle, α. Also shown are values from experiments by Ellison & Turner (1959) (●) along with their mean curve.

velocity, V_q, defined, following Ellison & Turner (1959), as

$$V_q = \int v^2 \, \mathrm{d}y \Big/ \int v \, \mathrm{d}y. \tag{6.4}$$

The flux gradient, $\mathrm{d}Q/\mathrm{d}x$, is obtained from the data in figure 18(a) as described above.

The sharp decrease between the two regions defined in § 4 is again apparent with E asymptoting downstream. Figure 20 show values of E for $x > 30$ cm plotted versus slope angle, α, along with data from the experiments by Ellison & Turner included for comparison. Also shown is their curve reflecting the mean of their measurements.

The data from the present experiments show considerable scatter but are generally higher than the Ellison & Turner measurements. The observed scatter in the data is a result of the positioning error discussed earlier, coupled with the intermittency of the entrainment process which we will discuss in the following section. Somewhat higher entrainment rates might be expected in the developing stages of the downslope flow due to the additional source of energy from the accelerating layer.

Although the flow is approaching a constant Richardson number, as evident in figure 6 and as is predicted by Ellison & Turner's theory, a core of dense, homogeneous fluid remains (figure 9) in the flowing layer. The flow has thus yet to attain a constant velocity as predicted by the theory. The acceleration of the dense core provides an additional energy source for the interfacial instability enhancing entrainment. The distance over which this dense core is entrained is estimated in § 7.4.

7. Discussion

The picture that arises of the developing shear layer in the high Richardson number region is that of a quasi-stable sheared density interface, with large-scale overturns restricted by buoyancy evident, while small-scale fluctuations persist, energized by the accelerating density current. It was observed in § 4.2 that the large-scale structure is essentially advected with the mean shear and furthermore that the frequency of the structures coincides with the buoyancy frequency (figure 17). Both of these observations can be accounted for by the description of the large-scale structure as a manifestation of a shear instability of the quasi-stable density interface. In fact, a simple argument using predictions from linear stability theory can show that the most unstable frequency of a quasi-stable interface occurs at N.

7.1. *The quasi-stable sheared interface*

Temporal linear stability analysis of a sheared density interface with equal density and velocity scales predicts a most unstable wavenumber occurring at $k\delta \approx 1$ (Hazel 1972), with a wavelength of $\lambda = 2\pi/k = 2\pi\delta$. Pawlak & Armi (1998) found that this scaling extends well to the spatially developing case. Spatial analysis of the shear profile with a sharp density interface gave a value of $k\delta \approx 1.2$. Further analysis (Pawlak 1997) has shown that the value approaches $k\delta \approx 1$ as the ratio of velocity to density layer thicknesses nears one and that the scaling is robust to the presence of a nearby boundary. This instability (Kelvin–Helmholtz) has an advective velocity essentially equal to the mean shear so that the frequency of the instability for the given wavenumber scaling is

$$f_\delta = \frac{2\pi}{\lambda}\left(\frac{\Delta U}{2}\right) = \frac{\Delta U}{2\delta}. \tag{7.1}$$

Now, with the observation that the downslope current rapidly reaches a steady, quasi-stable state with a constant bulk Richardson number, and assuming a value of $1/4$ for the critical Richardson number (equation (3.2)) we can substitute $\Delta U = 2\sqrt{g'\delta}$ in (7.1) to obtain

$$f_\delta = \sqrt{\frac{g'}{\delta}} = N. \tag{7.2}$$

This argument essentially notes that a shear layer becomes stable at the point where its most unstable frequency is lower than its associated buoyancy frequency. We argue then, that for the marginally unstable downslope current, the structures seen

in figures 11 and 12 and which result in the spectral peaks in figures 10 and 17, are manifestations of this shear instability at frequency, N. More significantly, perhaps, figure 12 shows evidence that the smaller, entraining scales are strongly correlated with this large-scale structure. This is consistent with the typical structure of shear instability, with higher gradients being concentrated in the high strain field of the nodal region between the cores of the cat's-eye structures (Corcos & Sherman 1984).

An alternative explanation for the observed structure is that it is a remnant of the initial instability. The evolution of the spectra in figure 10 might support this perspective since the frequency of the large scale appears near the second subharmonic of the initial instability. The structures would therefore result from a type of pairing of vortices generated by the initial pairing (figure 8). While this view cannot be discounted with the present data set, the coincidence of the measured large-scale frequency with the buoyancy frequency indicates that the large-scale structure has more significance. We have shown above how the frequency of the most unstable wavenumber in the near-stable shear layer is equal to the buoyancy frequency. The coincidence of the second subharmonic of the initial instability with N may accentuate its appearance. The comparable entrainment rates in the present set of experiments versus those measured by Ellison & Turner also suggest that entrainment mechanisms are related. This further supports the notion that the mechanism of small-scale mixing modulated by a large-scale instability is responsible for entrainment in a developed downslope current.

Further interesting features in the visualization in figure 12(*a*) are the apparent double-layer structures in the vorticity field. A speculative interpretation is that these may be associated with the cat's-eye structure of a shear instability, in particular since they appear to be correlated with the crests of the structure visible in the intensity sequence.

7.2. *Buoyancy-limited versus entraining scales*

One fundamental issue in the study of stratified turbulent flow involves the link between the buoyancy-dominated large scales, which represent the primary contribution to u_{rms} and the smaller-scale fluctuations associated with entraining motions. A useful comparison of the two scales is given by the ratio of entrainment velocity, $v_e = EV_q = \mathrm{d}Q/\mathrm{d}x$, to u_{rms}, plotted versus x in figure 21. The entrainment velocity is representative of the entraining motions and the ratio then illustrates the disparity between the scales of the motions. In the initial, rapid growth region, v_e is a significant fraction of u_{rms}. Farther downstream, the ratio drops significantly as the gap between the scales increases.

The variation of this ratio as a function of a Richardson number based on the large scales of the turbulence has been examined by a number of authors in a variety of flow configurations. Turner (1968) documented entrainment across a density interface due to grid-generated turbulence and observed a dependence of Ri^{-1} for large Richardson numbers and a dependence of $Ri^{-3/2}$ at moderate Ri. Experiments by Baines (1975), however, in which mixing was generated at an interface by a impinging jets and plumes showed a $Ri^{-3/2}$ relation. A range of experiments reviewed by Fernando (1991) show similar variations, yet the existence of these dependences on large-scale flow parameters highlights the link between the large and small scales. In any case, the variations in these relations between different flow configurations indicates distinct mechanisms for transfer of energy between the scales. Cotel & Breidenthal (1997) have suggested a model based on vortex persistence (advective time scale versus rotational time scale for the large scales) to account for the varied dependence

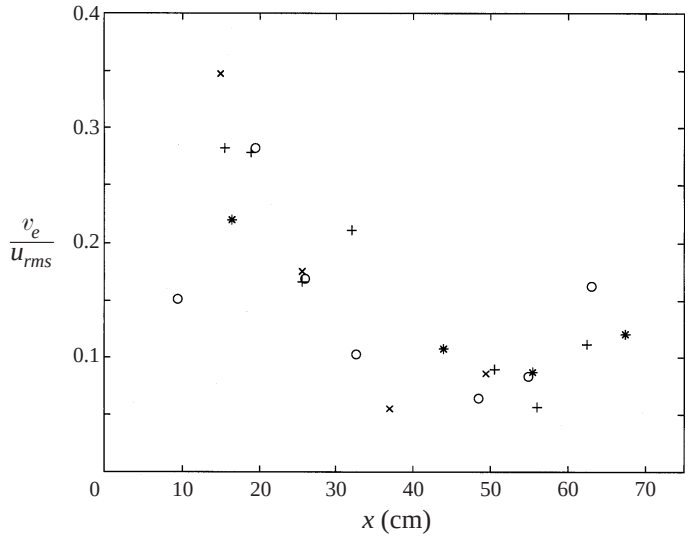

FIGURE 21. Entrainment velocity normalized by the maximum r.m.s. velocity fluctuations.

on Richardson number, Schmidt number and Reynolds number. Using dimensional arguments outlined in Appendix A, we suggest that a relation of

$$\frac{u'_e}{u'_{rms}} = Ri^{\frac{n+1}{2n+6}} \tag{7.3}$$

might be expected for downslope currents for sufficiently high Richardson and Reynolds numbers. In equation (7.3), n is the energy spectrum slope for the velocity fluctuations. This argument is consistent with the vortex persistence model and existing experimental data for a spectral slope of $-7/3$. The data in figure 17 are slightly steeper than -2 and could certainly be described by a slope of $-7/3$. The present data set is, unfortunately, ill-suited to verify this relationship, due to the small range of turbulent Richardson numbers attainable. This is partially a result of experimental limitations as well as inherent limits in Richardson number for downslope flows.

7.3. *Mixing intermittency*

A further complication in measurement of entrainment for the quasi-stable interface results from the inherent intermittency of entraining events. We have shown that the primary mechanism for instability is a large-scale shear instability which sets the stage for the growth of secondary turbulent structures at smaller scales. These appear to develop primarily in the high-strain nodal region of the larger scales. Vigorous entraining events then occur with a frequency equal to that of the large scales. Our measurements are limited to temporal sequences of about 90 s due to experimental constraints, which allow for the passage of only 7 or 8 large-scale events. This limitation accounts for much of the scatter in the measurements of interface thickness as well as in the entrainment estimates based on the gradients of the thickness.

The intermittency of the occurrence of mixing events also complicates the spectral argument discussed above and outlined in Appendix A. The implicit assumption in the use of a spectral decomposition is that there is a physical range of scales represented by the spectrum. The downslope current shows evidence, however, of a mechanism

S	δ_x	g'	H	E_1	E_2	Δx_1	Δx_2
0.068	0.1	1.75	10.7	0.07	0.025	26.8	157
0.125	0.1	1.75	10.7	0.16	0.020	26.8	86
0.188	0.1	1.75	10.7	0.10	0.035	26.8	57
0.250	0.1	1.75	10.7	0.10	0.040	26.8	43

TABLE 1. Flow parameters and estimated lengths for high and low entrainment regions.

for a discrete jump from large-scale to smaller entraining scales. For sufficiently high Reynolds numbers, the spectral slope is a measure of the rate of energy transfer between the scales, so the argument may remain relevant.

7.4. *Estimation of relaxation distance*

It is apparent in figure 6 that the flows considered are approaching a steady Richardson number as required by Ellison & Turner's theory. Unlike a fully developed downslope flow, however, the constant Richardson number is maintained by an increasing velocity, decreasing interface width and a constant density step. A secondary transition will be realized as the current entrains the remaining homogeneous fluid in the flowing layer. At this point, a steady Richardson number will be maintained by a balance between increasing δ and decreasing density step as observed by Ellison & Turner. With known rates of entrainment of dense fluid into the mixing layer, an estimate of the distance over which this transition will occur can be made. Ignoring the effects of the bottom boundary layer, this distance can serve as an estimate for the length over which the hydraulic flow relaxes to a downslope current. From the definition of entrainment given in equation (6.1),

$$\Delta x = \frac{\Delta Q}{EV}. \tag{7.4}$$

It was argued in § 4.1 that the length of the initial low Richardson number region, Δx_1, can be given by equation (4.3). Using this length in equation (7.4), along with the velocity scale, $V_0 \sim \sqrt{g'H}$, we find the portion of fluid entrained in the initial region to be

$$\frac{\Delta Q_1}{Q_i} = \frac{E_1}{4\delta_x}, \tag{7.5}$$

where $Q_i = H\sqrt{g'H}$ is the initial flow in the dense layer and E_1 is the upward entrainment in the initial region.

In the same manner, we can estimate the length of the high Richardson number region, Δx_2, before a fully developed downslope current is established. The velocity scaling is now somewhat complicated by the acceleration of the hydraulic flow. Using hydraulic theory for two-layer flow with an arrested upper layer (cf. Armi 1986; Pawlak & Armi 1997), we find

$$\frac{1}{V}\frac{\partial V}{\partial x} = -\frac{S/Y}{1-F^2}, \tag{7.6}$$

in which Y is the thickness of the flowing layer, $F^2 = V^2/g'Y$ is the layer Froude number and $S = \tan\alpha$ is the bottom slope (see figure 2*b*). As the flow accelerates, the layer Froude number increases rapidly, so we can make use of the fact that $F^2 \gg 1$

to expand equation (7.6) for small $1/F^2$. With this approximation, (7.6) becomes (ignoring higher-order terms)

$$\frac{\Delta V}{\Delta x} = \frac{g'S}{V_0} \tag{7.7}$$

and the velocity scale for the high Richardson number region is then given by

$$V = V_0 + \frac{g'S}{V_0}\Delta x. \tag{7.8}$$

This is equivalent to assuming that the increase in kinetic energy is equal to the decrease in potential energy over a distance, Δx, ignoring friction and limitations due to continuity.

Using (7.8) in (7.4),

$$\frac{\Delta Q_2}{Q_i} = \frac{E_2(V_0 + (g'S/V_0)\Delta x)\Delta x}{H\sqrt{g'H}} \tag{7.9}$$

with E_2 being the upward entrainment in the high Richardson number region. The entire flowing layer is entrained when $Q_i = \Delta Q_1 + \Delta Q_2$, therefore (7.9) yields

$$\frac{E_2}{H}\left(1 + \frac{S}{H}\Delta x\right)\Delta x = 1 - \frac{E_1}{4\delta_x}. \tag{7.10}$$

Solving for Δx,

$$\Delta x = -\frac{H}{2S} + \frac{1}{2}\left(\frac{H^2}{S^2} - \frac{4H^2(\delta_x - \frac{1}{4}E_1)}{E_2\delta_x S}\right)^{1/2}. \tag{7.11}$$

Estimated values for Δx_1, obtained from equation (4.3), and Δx_2, from equation (7.11), are given in table 1. The calculated values for the total distance $\Delta x_1 + \Delta x_2$ are somewhat longer than the length of the test section ($\sim$1 m) for the lower-slope cases while the higher-slope cases indicate that the developed flow, as we have defined it, is achieved within our observations. An alternative and perhaps more appropriate definition for the transition point is the location at which the shear and bottom boundary layers meet. At this point hydraulic acceleration ceases and the flow attains a constant velocity as observed by Ellison & Turner. Their estimate of $\Delta x \sim 10h_0$ is certainly met for the initial region of low Richardson number development. The approach to a steady velocity can be observed in the decreased slopes for the velocity data versus the theoretical curves in figure 3.

8. Summary and conclusions

This set of experiments has examined the transition from a hydraulically controlled wedge flow to a downslope current controlled by interfacial stress. Two distinct flow regions have been identified in the establishment of the downslope flow. The initial low Richardson number region is characterized by rapid growth of the mixing layer along with high entrainment. The vortex separation mechanism described in Pawlak & Armi (1998) is prevalent in the early stages, although the flow rapidly reaches a critical Richardson number which arrests the growth of the shear layer.

The low Richardson number region is limited to an extent of $O(H)$ and the flow approaches a quasi-stable state near the critical value of $Ri = 1/4$. The flow in the high Richardson number region shows evidence of persistent turbulent mechanisms. Spectral analysis and observations of temporal sequences have revealed large-scale

structures which are convected with the mean velocity and whose frequencies coincide with the buoyancy frequency, N. Using considerations from linear stability, it has been shown that this is the frequency of instability of the marginally unstable shear layer and on that basis the structure is described as a large-scale shear instability. We have also shown evidence that small entraining scales are correlated with the large-scale structure, occurring predominantly in the high strain nodal region.

Estimates of entrainment obtained for four experimental cases compare well with observations for developed downslope flows. This suggests that the observed entrainment mechanisms persist in the developed flow. The extent of both regions of the developing flow has been estimated as a function of bottom slope.

The Reynolds numbers in the developing region of the flows considered ranged from 2500 to 5300 based on the vorticity thickness. At these values we would expect considerable three-dimensional structure at the small scales. Since the observations are recorded within a small central slice of the channel we cannot consider these, except to note that the image sequences show clear evidence of small-scale out-of-plane motions. The large-scale structure remains two-dimensional, though, due to the primary vertical shear flow.

The effects of a turbulent bottom boundary layer have not been considered. In the cases studied here, the bottom boundary layer does not extend significantly into the stratified mixing layer. This factor will surely be of importance in downslope currents in real geophysical settings, particularly in cases where bottom-generated turbulence has an effect on interfacial mixing. Nonetheless, in situations where an inertial core of accelerating fluid persists, the phenomena discussed here will be relevant. This type of adjustment will also be important in zones where developed downslope currents are accelerated due to lateral constrictions and variations in bottom slope.

The experiments presented here were completed at Scripps Institution of Oceanography. Funding was provided by the Office of Naval Research and the National Science Foundation. We would like to express our gratitude to Juan Lasheras and Ken Melville for loans of various pieces of equipment and to Jochen Klinke for his technical assistance with imaging issues. We are grateful to our reviewers for careful and constructive comments on an earlier version of the paper. Special thanks are due to Parker MacCready, Eric D'Asaro and Robert Briedenthal for helpful insights and discussion.

Appendix. Spectral interpretation of entrainment slopes

Some insight into the link between large and small scales in an entraining stratified flow, as well as into the observed variation in entrainment versus Richardson number slope values can be gained by considering the scales in terms of spectral theory. For sufficiently high Reynolds numbers, velocity fluctuations at a given wavenumber, k, scale with the spectral energy, $\Phi(k)$, as $u' \sim (k\Phi(k))^{1/2}$ (Tennekes & Lumley 1972). We begin with the assumption that there is a range in the energy spectrum that can be scaled as $\Phi(k) \sim k^n$. For homogeneous turbulence, for example, an inertial subrange will have $n = -5/3$, again for sufficiently high Reynolds numbers. With this assumption, the velocity scaling, in terms of an associated length scale, $l' = k^{-1}$, is

$$u' \sim l'^{-(n+1)/2}. \tag{A 1}$$

First let us consider the case of entrainment across a sharp interface. If we define a Richardson number for the fluctuations, $Ri_{l'} = g'l'/u'^2$, and postulate that entrainment

will only occur for $Ri_{l'} < 1$ then we can write the critical entrainment velocity as

$$u'_e = (g' l'_e)^{1/2}. \tag{A 2}$$

If we assume, now, that the Richardson number of the flow is high enough that the entraining scales are significantly smaller than the large scales of the flow, from the scaling in (A 1), we can write

$$\frac{u'_e}{u'} \sim \left(\frac{l'_e}{l'}\right)^{-(n+1)/2} \tag{A 3}$$

and similarly (A 2) can be written

$$\frac{u'_e}{u'} = \frac{(g' l')^{1/2}}{u'} \left(\frac{l'_e}{l'}\right)^{1/2}. \tag{A 4}$$

Using (A 3) in (A 4) we obtain

$$\frac{u'_e}{u'} = \left(\frac{g' l'}{u'^2}\right)^2 \left(\frac{u'_e}{u'}\right)^{-1/(n+1)}. \tag{A 5}$$

Applying this relation for $u' = u'_{rms}$ and defining a Richardson number for the turbulence using u'_{rms} and its associated length scale (as in (5.2)) yields the following scaling:

$$\frac{u'_e}{u'} = Ri^{\frac{n+1}{2n+4}}. \tag{A 6}$$

This relation gives the dependence of the entrainment velocity on the bulk properties of the turbulence given a spectral shape along with the limiting effect of buoyancy on the entrainment.

For flows involving entrainment across an interface where the source of mixing is a homogenous turbulent flow, the spectral slope of $n = -5/3$ results in an exponent of -1 for the relation in (A 6). The vortex persistence model described by Cotel & Breidenthal (1997) predicts a relation of Ri^{-1} for this case with a multiplicative factor of $Sc^{-1/2}$ to account for diffusive effects. The variation of structure and entrainment for turbulent density interfaces due to diffusive effects was considered by Crapper & Linden (1974).

If we consider flows with diffuse interfaces, in which the entraining eddies are smaller than the interface thickness, then the critical entrainment velocity would be written instead as

$$u'_e = N l'_e. \tag{A 7}$$

Using (A 1) and (A 7), we find

$$\frac{u'_e}{u'} = Ri^{\frac{n+1}{2n+6}}. \tag{A 8}$$

For a spectral slope of -2, this would suggest a dependence of $Ri^{-1/2}$. Vortex persistence predicts a Ri^{-1} relation for diffuse interfaces at high Richardson and Reynolds numbers. A slope of $-7/3$ would be necessary to match this prediction using equation (A 8).

As the Richardson number diminishes, the gap between the large scales and the entraining scales decreases and the scaling argument we have used becomes more suspect.

REFERENCES

Armi, L. 1986 The hydraulics of two flowing layers with different densities. *J. Fluid Mech.* **163**, 27–58.

Armi, L. & Williams, R. 1993 The hydraulics of a stratified fluid flowing through a contraction. *J. Fluid Mech.* **251**, 355–375.

Baines, P. G. 1998 Downslope flows into a stratified environment-structure and detrainment. In *Mixing and Dispersion in Stably Stratified Flows, Proc. 5th IMA Conf. on Stratified Flows, Dundee*, pp. 1–21.

Baines, W. D. 1975 Entrainment by a plume or a jet at a density interface. *J. Fluid Mech.* **68**, 309–320.

Baringer, M. O. & Price, J. F. 1997 Mixing and spreading of the Mediterranean outflow. *J. Phys. Oceanogr.* **27**, 1654–1677.

Brown, G. L. & Roshko, A. 1974 On density effects and large structure in turbulent mixing layers. *J. Fluid Mech.* **64**, 775–816.

Corcos, G. M. & Sherman, F. S. 1976 Vorticity concentration and the dynamics of unstable free shear layers. *J. Fluid Mech.* **79**, 241–264.

Corcos, G. M. & Sherman, F. S. 1984 The mixing layer: deterministic models of a turbulent flow. Part 1. Introduction and the two-dimensional flow. *J. Fluid Mech.* **189**, 29–65.

Cotel, A. J. & Breidenthal, R. E. 1997 Persistence effects in stratified entrainment. *Appl. Sci. Res.* **57**, 349–366.

Crapper, P. F. & Linden, P. F. 1974 The structure of turbulent density interfaces. *J. Fluid Mech.* **65**, 45–63.

Ellison, T. H. & Turner, J. S. 1959 Turbulent entrainment in stratified flows. *J. Fluid Mech.* **6**, 423–448.

Farmer, D. M. & Armi, L. 1986 Maximal two-layer exchange over a sill and through the combination of a sill and contraction with barotropic flow. *J. Fluid Mech.* **164**, 53–76.

Farmer, D. M. & Armi, L. 1999 Stratified flow over topography: the role of small scale entrainment and mixing in flow establishment. *Proc. R. Soc. Lond.* A **455**, 3221–3258.

Fernando, H. J. S. 1991 Turbulent mixing in stratified fluids. *Ann. Rev. Fluid Mech.* **23**, 455–493.

Hazel, P. 1972 Numerical studies of the stability of inviscid stratified shear flows. *J. Fluid Mech.* **51**, 39–61.

Hopfinger, E. J. 1987 Turbulence in stratified fluids: a review *J. Geophys. Res.* **92**(C5), 5287–5303.

Koop, C. G. & Browand, F. K. 1979 Instability and turbulence in a stratified fluid with shear. *J. Fluid Mech.* **93**, 135–159.

Lilly, D. K. 1978 A serve downslope windstorm and aircraft turbulence event induced by a mountain wave. *J. Atmos. Sci.* **35**, 59–77.

Nieman, P. J., Hardesty, R. M., Shapiro, M. A. & Cupp, R. E. 1988 Doppler lidar observations of a downslope windstorm. *Mon. Wea. Rev.* **116**, 2265–2275.

Pawlak, G. 1997 Hydraulics, mixing and stability of a two-layer arrested wedge flow. PhD thesis University of California, San Diego.

Pawlak, G. & Armi, L. 1997 Hydraulics of a two-layer arrested wedge flow. *J. Hydr. Res.* **35**, 603–618.

Pawlak, G & Armi, L. 1998 Vortex dynamics in a spatially accelerating shear layer. *J. Fluid Mech.* **376**, 1–35.

Peltier, W. R. & Scinocca, J. F. 1990 The origin of downslope windstorm pulsations. *J. Atmos. Sci.* **47**, 2853–2870.

Tennekes, H. & Lumley, J. L. 1972 *A First Course in Turbulence*. MIT Press.

Thorpe, S. 1982 On the layers produced by rapidly oscillating a vertical grid in a uniformly stratified fluid. *J. Fluid Mech.* **124**, 391–409.

Turner, J. S. 1968 The influence of molecular diffusivity on turbulent entrainment across a density interface. *J. Fluid Mech.* **33**, 639–656.